A Comparative Analysis of the Boundary Condition Schemes for an Immersed Cylinder in a Water Stream with the Lattice Boltzmann Method

Flávio Hirai Garzeri[1], Ivan Talão Martins[1,2] and Luben Cabezas-Gómez[1,*]

[1] Heat Transfer Research Group, Department of Mechanical Engineering, São Carlos School of Engineering (EESC), University of São Paulo (USP), São Carlos, 13566-590, Brazil

[2] Campus Industrial de Ferrol, Universidade da Coruña (UDC), Rúa Mendizábal s/n, Ferrol, A Coruña, 15403, Spain

INFORMATION

Keywords:
Lattice Boltzmann method
circular cylinder flow
boundary conditions
von kármán vortex street
drag coefficient
external flow
curved boundaries
solid walls

DOI: 10.23967/j.rimni.2025.10.67648

SCIPEDIA Revista Internacional de Métodos Numéricos para Cálculo y Diseño en Ingeniería

Revista Internacional Métodos numéricos para cálculo y diseño en ingeniería RIMNI in cooperation with CIMNE

A Comparative Analysis of the Boundary Condition Schemes for an Immersed Cylinder in a Water Stream with the Lattice Boltzmann Method

Flávio Hirai Garzeri[1], **Ivan Talão Martins**[1,2] **and Luben Cabezas-Gómez**[1,*]

[1]Heat Transfer Research Group, Department of Mechanical Engineering, São Carlos School of Engineering (EESC), University of São Paulo (USP), São Carlos, 13566-590, Brazil

[2]Campus Industrial de Ferrol, Universidade da Coruña (UDC), Rúa Mendizábal s/n, Ferrol, A Coruña, 15403, Spain

ABSTRACT

In this paper, we investigate the performance of different boundary condition (BC) schemes for curved walls within the framework of the Lattice Boltzmann Method (LBM). A canonical benchmark problem—the flow past a circular cylinder in a channel—is considered, with Reynolds numbers ranging from 50 to 300. While prior studies have examined similar configurations, this work provides a novel comparative analysis under realistic conditions—using dimensional LBM simulations with actual fluid properties and consumer-grade hardware, rather than idealized lattice units. Additionally, we introduce an in-house GPU-accelerated solver, enabling efficient high-fidelity simulations without reliance on specialized computational resources. Four wall boundary conditions—the standard bounce-back scheme, the non-equilibrium extrapolation scheme, the fictitious equilibrium scheme and a one-point scheme—are implemented and analyzed through their influence on the time-averaged drag coefficient of the cylinder. The results are compared against both experimental and Navier-Stokes-based numerical data to assess accuracy. Additionally, the study evaluates the relative impact of outlet BC selection on simulation fidelity. The findings show that all tested solid wall boundary schemes can produce reasonable predictions under suitable conditions. Furthermore, based on our results, the accuracy of LBM simulations is notably more sensitive to the choice of the outlet boundary condition when compared to the choice of the ones used at the immersed body.

OPEN ACCESS

Received: 08/05/2025

Accepted: 24/06/2025

Published: 27/10/2025

DOI
10.23967/j.rimni.2025.10.67648

Keywords:
Lattice Boltzmann method
circular cylinder flow
boundary conditions
von kármán vortex street
drag coefficient
external flow
curved boundaries
solid walls

1 Introduction

Studying immersed bodies on a stream is relatively important for engineering purposes. Several civil and mechanical projects demand knowledge of the stresses caused by a stream around a body or the drag and lift forces acting on the same [1,2]. This phenomenon is characterized by the fluid-structure interaction, which depending on the situation can be a very challenging problem for prediction/modeling [3]. For this task, one can use theoretical approaches, numerical simulations,

*Correspondence: Luben Cabezas-Gómez (lubencg@usp.br).

or even experimental correlations, each having its own advantage depending on the request of the situation. In the case of numerical simulations, it allows for obtaining a complete and detailed description of the fluid flow and local stresses/forces on the immersed body, with relatively low cost in comparison to the experimental approach.

In this context, there are several numerical approaches in the literature [4,5]. For example, Mittal et al. [6,7] have numerically investigated he impact of an oscillating cylinder on the flow field. Between them, the lattice Boltzmann method (LBM) appears to be an attractive method, given its explicit characteristic and mesoscopic nature. The first point helps in dispensing the need of solving linear equation systems. The second gives the ability to deal with complex problems, such as multiphase problems [8–13], porous media flows [14–17], complex boundary conditions [18–20] or interfacial conditions [21–23]. Furthermore, the method performs its calculation steps locally in each node, making it highly suitable for parallel computing techniques [24–26]. Consequently, we can also find works in the literature regarding the use of LBM to simulate bodies immersed in fluid flow [27–30].

Nonetheless, there are some particular challenges when dealing with this problem with the LBM. The main question is how to deal with curved geometries. Since the LBM utilizes a uniform grid (the lattices), the physical boundaries of non-square geometries rarely fall into the locations of the lattice nodes [31]. Some initial works in literature proposed the approximation of these complex geometries by curved boundaries using stair-shaped steps [32–34]. Having the advantage of being simpler to implement, this kind of schemes can introduce inaccurate predictions of fluid flow.

In the sequence, other authors proposed the use of more complex schemes to better introduce the correct position of the boundary in the unknown populations (to be defined by the boundary conditions). For example, we have the fictitious equilibrium scheme (FES) proposed by Filippova and Hänel [35], where a fictitious equilibrium distribution function is calculated in the solid nodes and combined with the bounce-back scheme to better predict the effects of the wall which does not coincide with the lattice. Alternatively, Guo et al. [36] proposed an extrapolation model, the non-equilibrium extrapolation scheme (NEES), in which the non-equilibrium part of the distribution functions are extrapolated and used to calculate the unknown distribution functions at the curved boundary. Finally, some schemes were developed focused on the acceleration of BCs computation, as for example the one-point schemes (OP) [37], which use information available on a single node to calculate the unknown distribution functions.

For the last two decades, several works were developed considering the mentioned methods or even proposing new approaches [38–42]. Thus, it is interesting for the research community a quantitative comparison between the boundary condition schemes, to evaluate and determine the situations where one or other scheme is more suitable. In this context, the present study aims to extend the analysis of boundary condition schemes for curved geometries within the LBM framework, focusing on the four mentioned schemes: the standard bounce-back scheme (SBBS), the FES, the NEES and the one-point scheme (OP). Unlike previous comparative works [43,44], the present study addresses this comparison considering real fluids under real conditions. For this task, the dimensional form of the LBM, proposed by Martins et al. [45], is used in the simulations. This method eliminates the use of lattice units and allows the simulation to be performed directly using physical units.

Moreover, the results are compared with reference numerical results, as well as with experimental predictions from the open literature, allowing the validation of the numerical solutions from the present LBM. Another contribution addressed in the present work is that the present work addresses is the importance of choosing the correct outlet boundary condition when simulating a cylinder under a

stream in a channel. Our results show that some schemes of outlet BC scheme can introduce a suction force, changing the behavior of the simulation and deviating it from the expected results.

The paper is organized into three main sections. First, the methods employed are described in Section 2, as well as the boundary schemes used in the simulations. Next, the results are discussed in Section 3. Finally, the main conclusions of the paper are organized in Section 4.

2 Methods

2.1 The Latice Boltzmann Model

For this study, the dimensional approach for the LBM with the MRT collision operator was adopted [45]. As mentioned in Section 1, this approach dispenses the use of lattice units and allow the full simulation to be made using directly physical units. Here, we selected this approach because it facilitates the employment of real fluids on the simulations. The governing equation is shown in Eq. (1), where f_i corresponds to the density distribution functions in the discrete velocity direction i. Here, δt corresponds to the discrete time step and $\mathbf{c}_i$ the discrete particle velocity vector.

$$f_i(\mathbf{x}+\mathbf{c}_i\delta t, t+\delta t) - f_i(\mathbf{x},t) = -\mathbf{M}^{-1}\mathbf{S}\mathbf{M}\left[f_i(\mathbf{x},t) - f_i^{eq}(\mathbf{x},t)\right]\delta t \tag{1}$$

The equilibrium distribution functions, f_i^{eq}, are given in Eq. (2), which represents the density distribution functions at a state of local equilibrium. In this equation, c_s is the lattice sound speed and ω_i are lattice weights—which are respectively dependent on the chosen time step and lattice scheme. In our simulations, we employed the D2Q9 velocity scheme [46], thus $c_s = (\delta x/\delta t)\sqrt{1/3}$ and the respective weights are given by Eq. (3), while the discrete velocities, given by Eq. (4).

$$f_i^{eq}(\mathbf{x},t) = \omega_i \rho(\mathbf{x},t)\left[1 + \frac{\mathbf{c}_i\mathbf{u}}{c_s^2} + \frac{(\mathbf{c}_i\mathbf{u})^2}{c_s^4} - \frac{\mathbf{u}\cdot\mathbf{u}}{2c_s^2}\right]_{(\mathbf{x},t)} \tag{2}$$

$$\omega_i = \begin{cases} \dfrac{4}{9} & i = 0 \\ \dfrac{1}{9} & i = 1,\ldots,4 \\ \dfrac{1}{36} & i = 5,\ldots,8 \end{cases} \tag{3}$$

$$\mathbf{c}_i = \frac{\delta x}{\delta t}\begin{cases} (0,0) & i = 0 \\ (1,0),\ (0,1),\ (-1,0),\ (0,-1) & i = 1,\ldots,4 \\ (1,1),\ (-1,1),\ (-1,-1),\ (1,-1) & i = 5,\ldots,8 \end{cases} \tag{4}$$

To improve the stability of the method, the multiple-relaxation-time was used for the collision operator. This collision scheme maps the distribution functions into the moment space and, then, perform the collision. First, the moments of f_i are calculated using a transformation matrix M, as given by Eq. (5). Then, the collision is performed considering a collision matrix S, which contains the relaxation rates for each moment, as in Eq. (6). In the end, we obtain the post-collision distribution functions, $\tilde{f}_i$, using the inverse of the transformation matrix, as in Eq. (7).

The values of the relaxation rates were adopted following Lallemand and Luo [47], which are $S = [0, \tau_e^{-1}, \tau_\epsilon^{-1}, 0, \tau_q^{-1}, 0, \tau_q^{-1}, \tau^{-1}, \tau^{-1}]$. To keep the physical mean of the simulations and correctly recover the Navier-Stokes equation trough the Chapman-Enskog analysis, the viscous relaxation time is related to the viscosity of the fluid as $\nu = (\tau - \delta t/2)c_s^2$. In addition, according to Lallemand and

Luo [47] with the dimensional approach, we have $\tau_q^{-1} = (3/\delta t)(2/\delta t - \tau^{-1})/(3/\delta t - \tau^{-1})$. In this paper, the values used for the others relaxation times were equal to $1/\delta t$.

$$\mathbf{m}_k = \sum_i \mathbf{M}_{ki} f_i \quad \text{and} \quad \mathbf{m}_k^{eq} = \sum_i \mathbf{M}_{ki} f_i^{eq} \tag{5}$$

$$\tilde{\mathbf{m}}_k = \mathbf{m}_k - \mathbf{S}_k(\mathbf{m}_k - \mathbf{m}_k^{eq})\delta t \tag{6}$$

$$\tilde{f}_i = \sum_k \mathbf{M}_{ik}^{-1} \tilde{\mathbf{m}}_k \tag{7}$$

After this step, the populations are updated in accordance to the post-collision distribution functions, a process known as streaming, which can be represented by $f_i(\mathbf{x} + c_i\delta t, t + \delta t) = \tilde{f}_i(\mathbf{x}, t)$. The macroscopic fields, such as the density ρ and velocity u can then be recovered from the moments of the distribution function, as shown in Eq. (8). All the calculations mentioned in this section (collision, streaming and macroscopic variables calculation) are repeated for each time step, δt, until the desired time instant or the steady-state condition is is achieved.

$$\rho(\mathbf{x}, t) = \sum_i f_i(\mathbf{x}, t) \quad \text{and} \quad \rho(\mathbf{x}, t)\mathbf{u}(\mathbf{x}, t) = \sum_i \mathbf{c}_i f_i(\mathbf{x}, t) \tag{8}$$

2.2 Open Boundary Conditions

This section outlines the inlet and outlet boundary condition strategies used in the present study.

At the inlet, a modified bounce-back scheme is applied, which accounts for a specified inflow velocity u_{in} [48–50]. This method, often referred to as a velocity bounce-back, prescribes a uniform velocity profile at the inlet boundary. It is important to mention that the condition is only enforced on the population whose velocities points toward the inside of the computational domain, which are the populations whose values are not known during the streaming step. The formulation of this BC is shown at Eq. (9).

$$f_{\bar{i}}(\mathbf{x}_b, t + \delta_t) = f_i'(\mathbf{x}_b, t) - 2\omega_i \rho_{in} \frac{\mathbf{c}_i \cdot \mathbf{u}_{in}}{c_s^2} \tag{9}$$

At the outlet, common schemes often use a periodic condition with a prescribed pressure drop. However, this is not possible to use when the value of it is unknown to the user, such as the case analyzed in this study (see Section 3.1). Furthermore, since a prescribed input velocity is used in the opposite boundary, assuming the output to be periodic does not make sense. Alternative solutions have to be then employed in order bypass the problem of missing data. In this paper, two different outflow treatments have been considered.

The first is the Grad's approximation, adapted for the LBM [51] (see Eq. (10)), where Grad's closure and non-equilibrium thermodynamic concepts are employed to reconstruct the unknown populations, which are calculated as shown in Eq. (10) with respect to the momentum flux tensors $P_{\alpha\beta}$. Overall, it shows good stability and produces decent results, provided that the user is careful with the domain size [52].

$$f_{\bar{i}}(\mathbf{x}_b, t + \delta_t) = \omega_i \left[\rho + \frac{\mathbf{u}_\alpha \mathbf{c}_i}{c_s^2} + \frac{1}{2c_s^4}(\mathbf{P}_{\alpha\beta} - \rho c_s^2 \delta_{\alpha\beta})(\mathbf{c}_{i\alpha}\mathbf{c}_{i\beta} - c_s^2 \delta_{\alpha\beta)}) \right] \tag{10}$$
$$\mathbf{P}_{\alpha\beta} = \textstyle\sum_i f_i \mathbf{c}_{i\alpha}\mathbf{c}_{i\beta}$$

The second outlet BC analyzed in this paper is the anti-bounce-back approach [53], here, the sign of the populations are changed from the bounce-back approach, as seen in Eq. (11).

$$f_{\bar{i}}(\mathbf{x}_b, t+\delta_t) = -f_i'(\mathbf{x}_b, t) + 2\omega_i \rho_{out} \frac{\mathbf{c}_i \cdot \mathbf{u}_{out}}{c_s^2} \tag{11}$$

Differently from the inlet treatment, the velocity at the boundary ($\mathbf{u}_{out}$) is not known. Thus, a finite difference approximation is done: $\mathbf{u}_{out} = \mathbf{u}(\mathbf{x}_b) + \frac{1}{2}[\mathbf{u}(\mathbf{x}_b) - \mathbf{u}(\mathbf{x}_{b+1})]$, where $\mathbf{x}_b$ and $\mathbf{x}_{b+1}$ refer to the boundary node and the next interior node, following the inward normal vector of the boundary.

2.3 Boundary Conditions for Solid Walls

Due to the mesoscopic nature of the method, boundary conditions that are normally used in classical fluid dynamics and traditional CFD cannot be employed directly in the LBM. Instead, boundary treatments in LBM manipulate the distribution functions at the key nodes in the domain to ensure that macroscopic boundary conditions—such as the no-slip condition at solid walls—are correctly enforced when the macroscopic variables are recovered.

LBM boundary schemes generally fall into two categories: link-wise approaches, where boundaries are assumed to lie halfway between lattice nodes, and wet-node approaches, where boundaries are located directly on lattice nodes. In this work, we adopt the link-wise method, whose boundary treatments are known as bounce-back schemes.

2.3.1 Standard Bounce-Back

The standard (or simple) bounce-back (SBBS) rule is probably one of the most widely used boundary scheme in the LBM [48–50]. It dictates that if a distribution function f_i comes into contact with a solid wall, it is reflected back in the opposite direction at that same lattice node. Mathematically, this is shown in the Eq. (12).

$$f_{\bar{i}}(\mathbf{x}, t+\delta_t) = f_i(\mathbf{x}, t) \tag{12}$$

As mentioned before in Section 1, in the LBM the outline of curved geometries rarely align with the lattice nodes. As a consequence, when employing the bounce-back scheme to these kinds of geometries, the shape of them will be simplified by the expressions shown in the conditional Eq. (14) based on the distance ratio, Eq. (13) (see Fig. 1 for reference). This parameter is defined as the ratio between the distance of the boundary node and the physical boundary, $|x_f - x_w|$, and the distance between the boundary node and the next node inside the immersed body, $|x_f - x_s|$, which is usually equal to δx. This treatment was previously mentioned as well, that means that curved shapes will be treated as sequences of staggered stair steps.

$$q = \frac{|x_f - x_w|}{|x_f - x_s|} = \frac{|x_f - x_w|}{\delta x} \tag{13}$$

$$x_w = \begin{cases} q < 1/2: & x_f \\ q \geq 1/2: & x_s \end{cases} \tag{14}$$

Although this can degrade the accuracy of the model, one can still see the simplicity and the ease of implementation that this scheme offers, which makes it a popular choice between the boundary conditions of the LBM. Therefore, it is one of the approaches adopted in this study.

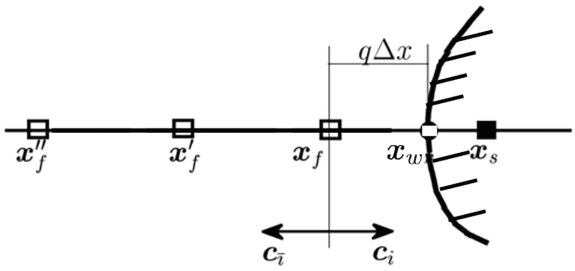

Figure 1: Representation of an immersed geometry with the notation of wall, solid and fluid nodes, from Guo and Shu [54]

2.3.2 *Fictitious Equilibrium Scheme*

First introduced by Filippova and Hänel [35], the fictitious equilibrium scheme (FES) is considered to be the earliest approach to account for the true shape of curved boundaries within the LBM framework. As the name implies, it creates a fictitious equilibrium distribution function at the solid nodes and combines it with the bounce-back scheme in order to form a post collision distribution function at this same node, which is shown in Eq. (15).

$$f'_{\bar{i}}(\mathbf{x}_s, t) = (1-\chi) f'_i(\mathbf{x}_f, t) + \chi f^*_i(\mathbf{x}_s, t) - 2\omega_i \rho(\mathbf{x}_f, t) \frac{c_i \cdot \mathbf{u}_w}{c_s^2} \tag{15}$$

Here, f^*_i corresponds to the fictitious equilibrium function and is given in Eq. (16), χ is the weighting factor and u^* is the interpolated velocity; both which are dependent on q, as shown in Eq. (17). It is important to mention that the parameter χ has the role of interpolator factor for the unknown distribution functions, which also must account for the collision consequence. This is the reason why it is dependent on both q (spatial interpolation) and τ (collision process).

$$f^*_i(\mathbf{x}_s, t) = \omega_i \rho(\mathbf{x}_f, t) \left[1 + \frac{\mathbf{c}_i \cdot \mathbf{u}^*}{c_s^2} + \frac{\mathbf{c}_i \cdot \mathbf{u}_f{}^2}{2c_s^4} - \frac{\mathbf{u}_f{}^2}{2c_s^2} \right] \tag{16}$$

$$\begin{cases} q < 1/2: & \mathbf{u}^* = \mathbf{u}_f, \quad \chi = \dfrac{2q-1}{\tau - 1} \\ q \geq 1/2: & \mathbf{u}^* = \frac{q-1}{q}\mathbf{u}_f + \dfrac{1}{q}\mathbf{u}_w, \quad \chi = \dfrac{2q-1}{\tau} \end{cases} \tag{17}$$

This approach better respects the curvature of walls, and should improve accuracy compared to the standard bounce-back.

2.3.3 *Non-Equilibrium Extrapolation Scheme*

Proposed by Guo et al. [36], the non-equilibrium extrapolation scheme extends the ideas of the fictitious equilibrium method. It uses the same methodology adopted in the previous scheme of constructing post-collision distribution functions at the solid nodes. However, it also performs a collision step in the solid nodes, which will then be propagated to the fluid nodes at the streaming step.

Here, the distribution functions at the solid nodes are separated in its equilibrium and non-equilibrium parts, a process shown at Eqs. (18) and (19).

$$f_{\bar{i}}(\mathbf{x}_s, t) = f_i^{(eq)}(\mathbf{x}_s, t) + f_i^{(neq)}(\mathbf{x}_s, t) \tag{18}$$

$$f_{\bar{i}}^{(eq)} \approx f_{\bar{i}}^{*}(\mathbf{x}_s, t) \equiv \omega_{\bar{i}}\rho(\mathbf{x}_f, t)\left[1 + \frac{\mathbf{c}_{\bar{i}}\cdot\mathbf{u}_s}{c_s^2} + \frac{\mathbf{c}_{\bar{i}}\cdot\mathbf{u}_s^{\,2}}{2c_s^4} - \frac{\mathbf{u}_s^{\,2}}{2c_s^2}\right] \tag{19}$$

The velocity at the solid node $\mathbf{u}_s$ depends on the value of q and is given by Eqs. (20) and (21).

$$u_s = \begin{cases} q \geq 3/4: & \mathbf{u}_{s1} \\ q < 3/4: & q\mathbf{u}_{s1} + (1-q)\mathbf{u}_{s2} \end{cases} \tag{20}$$

$$\mathbf{u}_{s1} = \frac{1}{q}\mathbf{u}_w + \frac{q-1}{q}\mathbf{u}(\mathbf{x}_f), \qquad u_{s2} = \frac{2}{q+1}\mathbf{u}_w + \frac{q-1}{q+1}\mathbf{u}(\mathbf{x}_f') \tag{21}$$

The non-equilibrium part is given in a similar way by Eq. (22).

$$f_{\bar{i}}^{(neq)}(\mathbf{x}_s, t) = \begin{cases} q \geq 3/4: & f_{\bar{i}}^{(neq)}(\mathbf{x}_f, t) \\ q < 3/4: & qf_{\bar{i}}^{(neq)}(\mathbf{x}_f, t) + (1-q)f_{\bar{i}}^{(neq)}(\mathbf{x}_f', t) \end{cases} \tag{22}$$

Finally, the post collision distribution function in the solid node is given by the Eq. (23).

$$f_{\bar{i}}'(\mathbf{x}_s, t) = f_{\bar{i}}(\mathbf{x}_s, t) - \frac{1}{\tau}f_{\bar{i}}^{(neq)}(\mathbf{x}_s, t) = f_{\bar{i}}^{*}(\mathbf{x}_s, t) + \frac{\tau-1}{\tau}f_{\bar{i}}^{(neq)}(\mathbf{x}_s, t) \tag{23}$$

This approach also offers greater accuracy when compared to the SBBS, and can be used for flat surfaces as well.

2.4 One-Point Curved Scheme

Proposed by [37], this scheme presents a novelty in the sense that it ends up using information of only a single node in the process of defining the values of the unknown distribution functions. Furthermore, it doesn't use a conditional statement with respect to the value of q in the process. From a practical perspective, this means that this scheme ends up being faster than the aforementioned ones, which justifies its intended use case: complex particulate flows.

Its formula employs a combination of the distribution functions at the nodes $\mathbf{x}_f'$ and $\mathbf{x}_w$, as shown in Eq. (24). The main process behind this scheme consists in approximating the parts that compose this formula into information that is known about the node x_f.

$$f_i(\mathbf{x}_f, t+\delta_t) = \frac{1}{1+q}(f_i(\mathbf{x}_w, t+\delta_t) + qf_i(\mathbf{x}_f', t+\delta_t)) \tag{24}$$

Beginning with the part correspondent to the nearest fluid node, one can simply use the post collision distribution function at the node $\mathbf{x}_f$, in accordance to Eq. (25). The wall part is decomposed in its equilibrium and non-equilibrium parts, the first is approximated in the way shown in Eq. (26), whereas the other is shown in Eq. (27).

$$f_i(\mathbf{x}_f', t+\delta_t)) = f_i'(\mathbf{x}_f, t) \tag{25}$$

$$f_i^{(eq)}(\mathbf{x}_w, t+\delta_t)) \approx f_i^{(eq)}(\mathbf{u}_w(t+\delta_t), \rho_{\mathbf{x}_f}(t)) \tag{26}$$

$$f_i^{(neq)}(\mathbf{x}_w, t+\delta_t)) \approx f_{\bar{i}}^{(neq)}(\mathbf{x}_f, t) \tag{27}$$

Given that we will be dealing with a stationary obstacle, the final simplified formula of the unknown populations are shown in Eq. (28).

$$f_i(\mathbf{x}_f, t+\delta_t) = \frac{1}{1+q}\left(\omega_i \rho_{\mathbf{x}_f}(t) + f_{\bar{i}}^{(neq)}(\mathbf{x}_f, t)) + q f_i'(\mathbf{x}_f, t)\right) \tag{28}$$

2.5 *Hardware and Software*

A general solver was programmed using the CUDA/C++ API, where individual kernel functions were assigned for each step of the method (collision, streaming, application of BCs and macroscopic variables update). The hardware used consisted of a workstation having a AMD Ryzen® Threadripper 7970X as the CPU and a Nvidia Geforce® RTX 4070Ti Super as the GPU, running Ubuntu 24.04 as the OS.

3 Results and Discussion

3.1 *Case Studied*

To assess the performance of the various boundary condition (BC) schemes, we choose a well explored general case: the flow around a circular cylinder in the center of an open channel. This configuration has been studied extensively in the literature, through both experiments [55,56] and numerical simulations [57–59], some of which also employs the lattice Boltzmann method [19,60].

A notable characteristic of this flow, particularly at moderate values of the Reynolds number ($Re \leq 300$), is the development of the Von Kármán vortex street—a periodic shedding of alternating vortices downstream of the cylinder. The Reynolds number itself is given in relation to the cylinder diameter and with the inlet velocity, as shown in Eq. (29).

$$Re = \frac{U_{in} D}{\nu} \tag{29}$$

In our simulations, the ratio between the cylinder diameter and channel width (also known as the blockage ratio) was maintained at a constant value of 0.1, as illustrated in Fig. 2. Since we use a dimensional LBM approach, all physical quantities are directly used in physical units, without the necessity of conversion to lattice units. The working fluid in the simulations corresponds to water at 25°C. The complete set of physical parameters employed in the simulation is presented in Table 1 alongside its respective values.

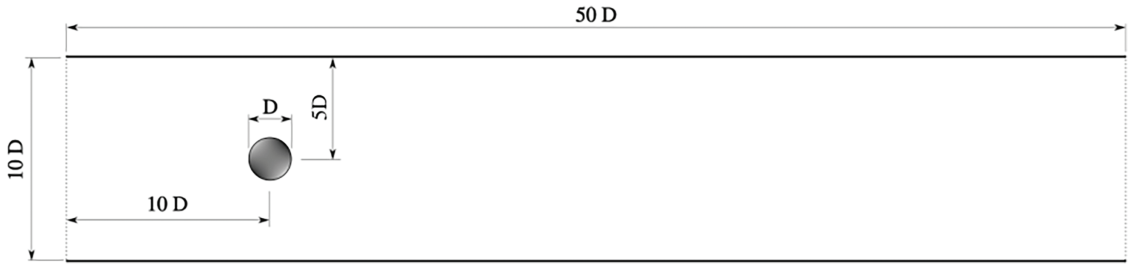

Figure 2: Diagram showing the relative dimensions of the channel

In order to evaluate the performance of the model, we focus on two different quantities that are widely studied in this type of flow: the drag coefficient (C_d) and the lift coefficient (C_l). These are calculated by dividing the magnitude of the appropriate component of the force vector by the dynamic pressure times the cylinder diameter, as shown in Eq. (30). For C_d, the force component along the

channel direction is used, whereas for C_l, the component perpendicular to the channel is considered.

$$C_d = \frac{2F_x}{\rho U_{in}^2 D} \quad , \quad C_l = \frac{2F_y}{\rho U_{in}^2 D} \tag{30}$$

Table 1: Simulation parameters-Fixed cylinder

Physical variable name	Variable value
Channel width (W)	0.3 (m)
Channel length (L)	1.5 (m)
Cylinder diameter (D)	3 (cm)
Relaxation time (τ)	0.60
Fluid density (ρ)	997.05 (kg/m^3)
Kinematic viscosity (ν)	$8.917e{-}7$ (m/s)

An important consideration arises regarding how to calculate the force acting on a immersed boundary using the LBM. One way is to sum all the hydrodynamic stresses (viscous stresses and pressure) acting on the nodes in the vicinity of the body surface [35]. Although this method produces reasonable results, in this work we adopt the momentum exchange method [48,49], chosen for its simplicity and proven accuracy [27].

The momentum exchange method employs the impulse theorem, which calculates the force based on the change in the linear momentum of populations that interact with the immersed boundary. The method is described in Eqs. (31) and (32).

$$\Delta \mathbf{Q} = {\delta_x}^2 \sum_{\mathbf{x}_w} \mathbf{c}_i [f'_{\bar{i}}(\mathbf{x}_s, t) + f'_i(\mathbf{x}_f, t)] \tag{31}$$

$$\mathbf{F} = \frac{\Delta \mathbf{Q}}{\delta t} \tag{32}$$

3.2 GPU Parallelized Code

As mentioned in Section 1, we use the Nvidia CUDA API to parallelize our simulation code. The strategy is straightforward: each step of the standard LBM approach is implemented as a GPU kernel. All kernels run with 256 threads arranged in a 16×16 square grid, which proved effective for our results.

The code begins by allocating all simulation variables in the GPU's global memory. Key physical quantities—such as velocity, pressure, and force—also have corresponding arrays in the host memory to allow tracking at each time step. Constant values are then defined, including transformation matrices used by the MRT collision operator.

Next, three initial GPU kernels are executed. The first identifies solid nodes based on the cylinder's size and position using a boolean object matrix. The second initializes the domain populations with their equilibrium values. The third calculates the q variable on boundary nodes near the stationary cylinder. Since the boundary is fixed, these values remain constant throughout the simulation.

The main LBM loop then begins with the collision step using the MRT operator. Its kernel has three loops over velocity directions (i): the first updates equilibrium distribution functions, the second

performs the collision in momentum space, and the third returns results to the population space. Post-collision values are stored in a separate array to avoid data conflicts.

The streaming kernel updates population values based on the post-collision data. Then, three boundary condition kernels are applied: one for inlet and outlet, another for side walls, and a third for the cylinder surface. Finally, a kernel computes the macroscopic variables, completing the iteration.

After several time steps, two final tasks are performed: calculating the force on the cylinder and recording macroscopic variables for analysis. These are done at user-defined intervals, corresponding to four data sets per second of simulation time. At each interval, a dedicated GPU kernel computes the force using Eq. (32). Then, macroscopic variables are transferred to host memory and saved in .csv files for further analysis.

3.3 First Results and Convergence Test

Following this setup, we conduct the first series of simulations. Boundary conditions are applied as follows: bounce-back at both the inlet and channel walls, and Grad's extrapolation at the outlet. Fig. 3 presents a velocity field visualization for $Re = 250$, in which the Von Kármán vortices can be clearly visualized. The oscillatory pattern observed at the velocity field is also reproduced on the instant values of C_d and C_l, as we can see in Fig. 4, also for $Re = 250$.

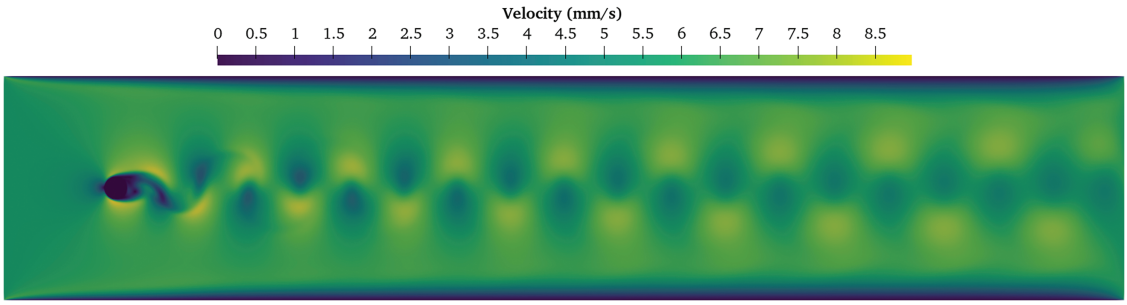

Figure 3: Velocity scale for $Re = 250$ and $t = 750\,\text{s}$

Regarding Fig. 4, from the oscillatory behavior we can calculate the average values of the lift and drag coefficients, which are displayed by the dotted lines. The average value of C_l is zero for all ranges of tested Re, which is expected giving its symmetric placement within the flow channel. Thus, our analysis will focus on the average of C_d.

Before proceeding with any type of validation or review of the usability of the model, we first perform a convergence check in relation to the grid resolution. This is done by keeping the parameters of Table 1 constant and maintaining the channel geometry of Fig. 2, while increasing the number of nodes used in the simulations. By doing these steps, the value of δx is determined by the relation $\delta x = W/N_y$, with N_y being the number of nodes across the width of the channel. Furthermore, the value of the time step (δt) is calculated in order to keep the same relaxation time in the simulations, keeping the relation between τ and ν previously stated in Section 2. Thus, as consequence, the simulated domain, as well as the fluid properties were kept the same, and only the values of δx and δt were changed.

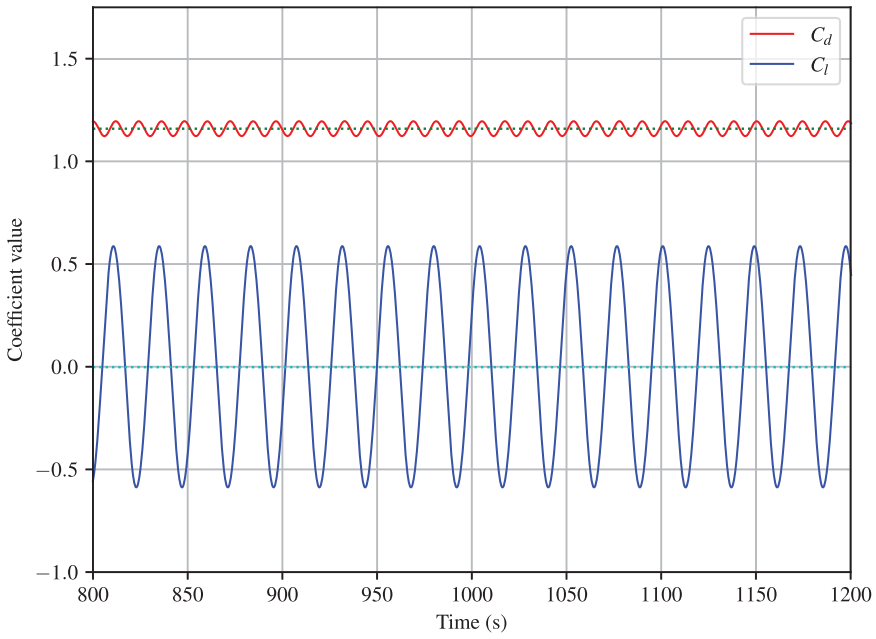

Figure 4: Values of C_l and C_d through a time range from $t = 800$ (s) and $t = 1200$ (s) for $Re = 250$

The results for the grid convergence analysis are shown in Fig. 5 for $Re = 50$. The first tests had been performed with $N_y = 128$ and have received increments of 128 up to $N_y = 768$. The results refer to the percentage difference between the average C_d in each mesh size when compared to that obtained when $N_y = 768$, adopted as our reference solution. Overall, it is possible to see that all four boundary condition schemes demonstrate convergence towards a common value. This indicates that, indeed, the solution depends on the grid resolution used to simulate the problem. However, the results for higher grids presented errors lower enough to be considered good results. In addition, both the standard bounce-back boundary condition and the one-point scheme exhibits greater inaccuracies at lower values of N_y in comparison to the other boundary schemes. This is an expected occurrence since the bounce-back method does not accurately capture the true curvature of the cylinder, leading to greater geometric roughness (stair-step effects) when δx is relatively large.

The grid convergence test showed that for resolutions above 384 nodes the results converged properly, although the OP scheme presents a little bit of fluctuation from the results at $N_y = 384$ and $N_y = 512$. Nonetheless, we perform the further analysis of this paper considering a grid size of 768 lattices in the y direction.

3.4 Drag Coefficient Analysis

To evaluate the influence of different boundary condition (BC) schemes on the drag coefficient, a series of simulations were performed over a Re range from 50 to 300. This range was selected because it encompasses the onset and development of the Von Kármán vortex street. The computational domain was fixed at 3840 lattice units in length and 768 in width. The mean drag coefficient was calculated over the interval $t = 1250$ s to $t = 1500$ s, a period during which the flow exhibited a stable periodic regime. The time step here has a value of $\delta t \approx 0.00570$ s and the discrete space interval is $\delta x \approx 0.00039$ m.

In order to assess the different boundary conditions applied at the cylinder surface, each scheme shown in Section 2 was tested, keeping the other BC (top, bottom, inlet and outlet) unchanged. The results are presented in Fig. 6, alongside reference data from the literature, which includes results from experiments [61] and conventional Navier-Stokes based numerical simulations [57,58].

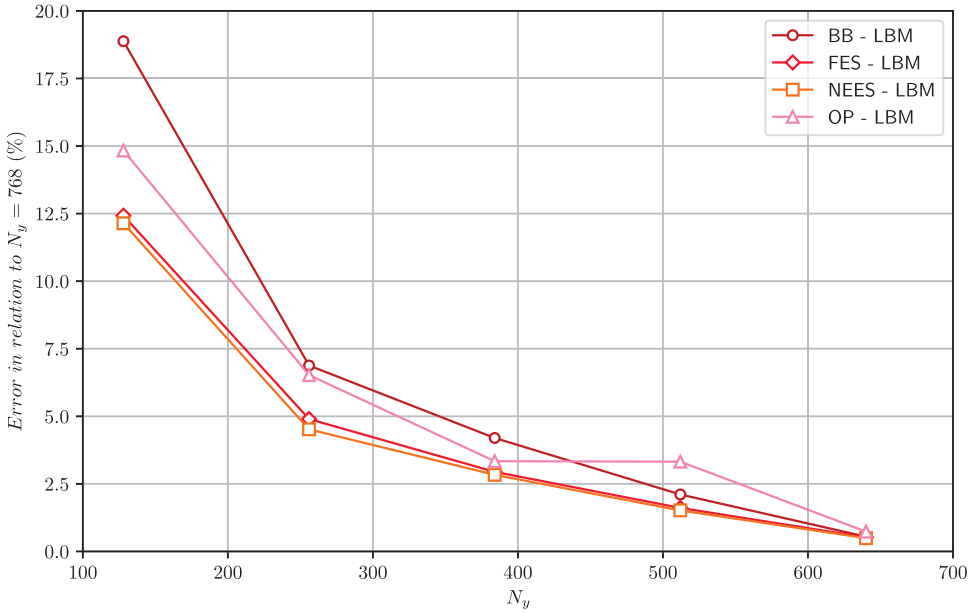

Figure 5: Grid convergence analysis for the selected boundary conditions at $Re = 50$

Overall, it is possible to see that three of the BC schemes demonstrated similar qualitative behavior: SBBS, FEQ and NEES, where the C_d decreases as the Reynolds number increases. The FEQ and NEES yielded nearly identical results, while the bounce-back scheme exhibited systematically lower C_d values. Meanwhile, the OP scheme produced the most different results when compared to the other BCs. While it also had the same behavior in general relation between the C_d and the Reynolds, this scheme produced a significant valley from the values of $Re = 100$ up to $Re = 150$. Furthermore, it produced the lowest values of the drag coefficient across all of our tested values, even lower than those produced by the SBBS.

A velocity profile was plotted for each boundary condition at Reynolds number 125, chosen for its noticeable differences between BCs—especially the OP scheme. All plots use a time step of $t = 1500$ (s) and the same simulation parameters as in previous results. The plots are available in Appendix A. Overall, the differences between profiles are subtle. A small phase shift is observed between boundary conditions, with the OP scheme showing the most pronounced offset. This justifies the choice of average C_d as the main parameter in our analysis.

Despite these discrepancies, the numerical predictions are in a good concordance between the experimental and the numerical references, where the results end up falling between them. The relative errors (norm L1) of the numerical results in comparison to the experimental data is reported in Table 2 for the values of Re tested. The largest error was observed at the same Re value for three of the BC schemes—SBBS, FEQ and NEES—at about $Re = 50$. For this occasion, the average error was 4.41%, 4.90% and 4.95% for the bounce-back, FEQ and NEES schemes, respectively. Furthermore, for Reynolds numbers ranging from 100 to 300—where vortex shedding becomes more pronounced

— the mean errors decreased to 3.6% (BB), 3.34% (FEQ), and 3.40% (NEES). On the other hand, OP had its highest error at $Re = 125$, being of 14.41%, while its average error was of 6.12%.

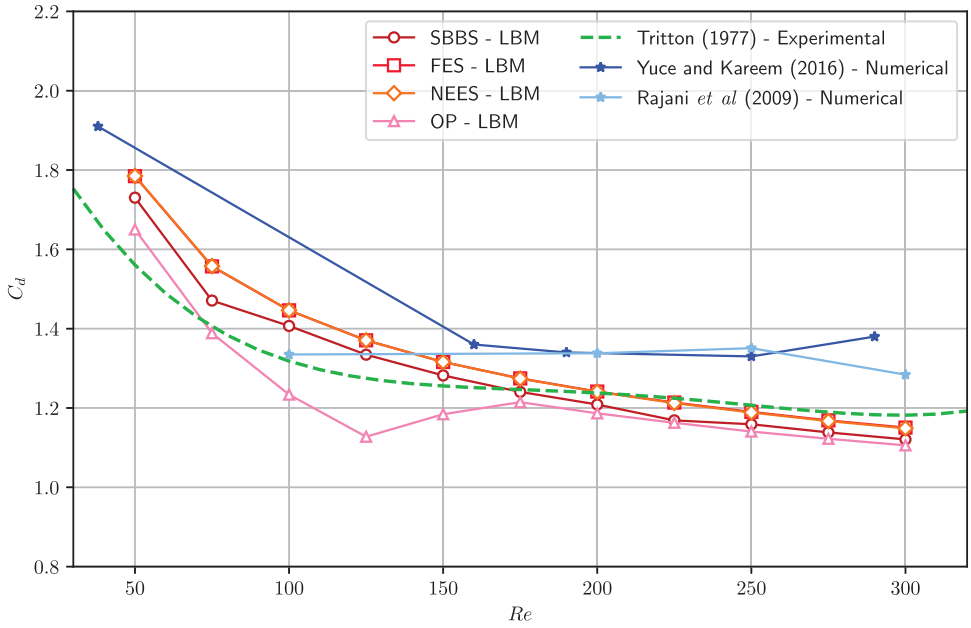

Figure 6: Comparison between the selected boundary conditions with numerical and experimental data available in the literature [57,58,61]

Table 2: Difference between the LBM simulations and the experimental results

Reynolds number	BB	FEQ	NEES	OP
50	11.00%	13.70%	13.73%	6.67%
75	4.82%	10.08%	10.13%	0.83%
100	5.46%	8.03%	8.04%	7.80%
125	3.33%	5.88%	5.87%	14.41%
150	1.72%	4.25%	4.26%	6.40%
175	0.05%	2.72%	2.67%	2.08%
200	1.76%	0.92%	0.88%	3.67%
225	4.38%	0.52%	0.62%	4.93%
250	4.40%	1.67%	1.80%	6.09%
275	5.41%	2.68%	2.82%	6.92%
300	6.18%	3.43%	3.59%	7.62%

The larger errors observed for low Re values can be connected to a higher difficulty of modeling the phenomenon for low flow velocities. Consequently, any numerical errors/deviations, or interferences in the case of the experiment, can anticipate the transition of the flow to an oscillatory behavior. Thus, more deviations between the numerical and the reference results are already expected. Also,

the two reference numerical data from literature deviates more in this region, in comparison to the experimental results.

Interestingly, the bounce-back scheme produced the lowest average error compared to the experimental correlation of Tritton [61]. However, FEQ and NEES results aligned more closely with those from previous numerical studies, suggesting greater consistency with established simulation frameworks.

3.5 Impact of the Outlet Boundary Condition

Following the initial drag analysis, we decided to change the outlet BC in order to assess its influence on the overall results. For this task, we also used the drag coefficient as the main parameter of the analysis, and all physical variables and simulation parameters of Table 1 were kept the same. The only change was the substitution of Grad's extrapolation scheme by the anti bounce-back scheme, as described in Section 2, in order to investigate the effects of this change. The results obtained with this new outlet BC, alongside those obtained with Grad's approximation, are shown in Fig. 7.

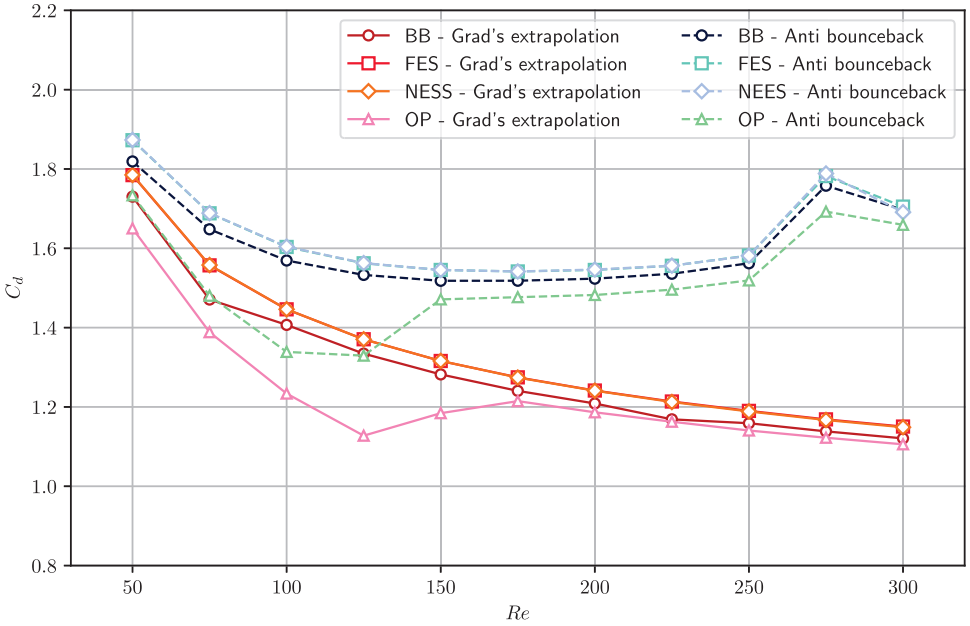

Figure 7: Comparison between the results of the LBM simulations using the anti-bounce-back scheme at the outlet with the previous results using the Grad's extrapolation scheme

Analyzing the results, we realize that the anti-bounce-back scheme consistently produced higher drag coefficients than Grad's extrapolation. This discrepancy can be attributed to fundamental differences on the way that each scheme handles the unknown distribution functions at the outlet. Grad's extrapolation, for example, employs approximations based on the kinetic theory to reconstruct the unknown distribution functions, whereas the anti-bounce-back scheme imposes a fixed pressure condition that can induce a suction effect. Depending on the specified outlet pressure (specified by the outlet imposed density, ρ_ω), this can cause a significant pressure drop, influencing the force experienced by the immersed body (the cylinder, in our case).

These findings illustrate that the choice of the outlet boundary condition may exert a greater influence on aerodynamic coefficients than the boundary conditions applied directly at the surface of the immersed object.

4 Conclusions

In this work, a novel methodology using dimensional LBM simulations with actual fluid properties was employed in order to analyze four types of boundary conditions within the LBM framework, all of them applied to the surface of an immersed cylinder. The main parameters used for the comparison were the drag and lift coefficients, considering a range of Reynolds numbers between $Re = 50$ and 300. The study revealed that all schemes captured the general decreasing trend of the drag coefficient with increasing Reynolds number.

In this work, we restricted ourselves to low Re numbers in order to guarantee that the 2D approach employed here is enough to capture the phenomenon with a considerable precision. The comparison between the simulation results and the reference data confirmed the veracity of the previous affirmation. For higher values of Re, a 3D approach, as well as the use of a turbulence model should be considered, in order to have a more complete description of the phenomenon.

However, the FEQ and NEES schemes produced better results in comparison to previous Navier-Stokes-based numerical data, presenting also almost identical results. The standard bounce-back method, while less accurate particularly at lower grid resolutions, exhibited the smallest average error when compared directly with experimental drag values from the literature. This highlights a trade-off between physical fidelity and numerical convenience when selecting boundary treatments for curved geometries.

Additionally, the study examined the impact of the outlet boundary condition on the results. For this, we compared Grad's extrapolation scheme with the anti-bounce-back pressure-based scheme. The results revealed that the anti-bounce-back scheme can induce a suction of the fluid at the outlet, changing the measured values of C_d and inserting deviations from the expected results. Thus, we can conclude that the outlet BC can exert a non-negligible influence on the computed aerodynamic forces, often surpassing the effect of the boundary condition applied at the surface of the body.

In general, all tested methods are capable of producing reasonable predictions under appropriate conditions. Nonetheless, the choice of boundary condition—both at the solid interface and at the outlet—plays a crucial role in the accuracy of LBM simulations. For high-fidelity aerodynamic predictions, particularly at lower Reynolds numbers or under coarse discretizations, more refined schemes such as FEQ or NEES combined with physically-consistent outlet treatments are recommended.

Acknowledgement: Not applicable.

Funding Statement: The authors acknowledge the support received from FAPESP (São Paulo Research Foundation), grants 2022/15765-1 and 2023/02383-6, and CNPq (National Council for Scientific and Technological Development), process 305771/2023-0 and 131776/2023-1.

Author Contributions: The authors confirm contribution to the paper as follows: Conceptualization, Flávio Hirai Garzeri, Ivan Talão Martins and Luben Cabezas-Gómez; investigation, Flávio Hirai Garzeri; resources, Luben Cabezas-Gómez; methodology, Flávio Hirai Garzeri and Ivan Talão Martins; data curation, Flávio Hirai Garzeri; software, Flávio Hirai Garzeri and Ivan Talão Martins; validation, Flávio Hirai Garzeri; writing—original draft preparation, Flávio Hirai Garzeri and

Ivan Talão Martins; writing—review and editing, Ivan Talão Martins and Luben Cabezas-Gómez; visualization, Luben Cabezas-Gómez; supervision, Luben Cabezas-Gómez; project administration, Luben Cabezas-Gómez; funding acquisition, Luben Cabezas-Gómez. All authors reviewed the results and approved the final version of the manuscript

Availability of Data and Materials: Data available within the article.

Ethics Approval: Not applicable.

Conflicts of Interest: The authors declare no conflicts of interest to report regarding the present study.

References

1. Jones RT. Classical aerodynamic theory. Washington, DC, USA: National Aeronautics and Space Administration; 1979.
2. Morand HJP, Ohayon R. Fluid-structure interaction: applied numerical methods. Hoboken, NJ, USA: Wiley; 1995.
3. Zhang J, Chen M, Shen B, Zhang D, Cheung SCP. Numerical approaches to capture fluid-structure interaction considering interfaces for offshore structures. Int J Fluid Eng. 2025;2(2):020601. doi:10.1063/5.0226161.
4. Hou G, Wang J, Layton A. Numerical methods for fluid-structure interaction—a review. Commun Comput Phys. 2012;12(2):337–77. doi:10.4208/cicp.291210.290411s.
5. Kim W, Choi H. Immersed boundary methods for fluid-structure interaction: a review. Int J Heat Fluid Flow. 2019;75:301–9. doi:10.1016/j.ijheatfluidflow.2019.01.010.
6. Mittal HVR, Ray RK, Al-Mdallal QM. A numerical study of initial flow past an impulsively started rotationally oscillating circular cylinder using a transformation-free HOC scheme. Phys Fluids. 2017;29(9):093603. doi:10.1063/1.5001731.
7. Mittal HVR, Al-Mdallal QM. A numerical study of forced convection from an isothermal cylinder performing rotational oscillations in a uniform stream. Int J Heat Mass Transfer. 2018;127(1):357–74. doi:10.1016/j.ijheatmasstransfer.2018.07.022.
8. Huang H, Sukop MC, Lu XY. Multiphase lattice boltzmann methods: theory and applications. Hoboken, NJ, USA: John Wiley & Sons, Ltd.; 2015.
9. Martins IT, Gómez LC, Alvariño PF. Parametric investigation of Rayleigh-Taylor instability under experimental conditions with the lattice Boltzmann method. Phys Fluids. 2025;37(2):024131. doi:10.1063/5.0256018.
10. Guzella MDS, Cabezas-Gómez L. Pseudopotential lattice boltzmann method simulation of boiling heat transfer at different reduced temperatures. Fluids. 2025;10(4):90. doi:10.3390/fluids10040090.
11. Martins IT, Fariñas Alvariño P, Cabezas-Gómez L. A new methodology for experimental analysis of single-cavity bubble's nucleation, growth and detachment in saturated HFE-7100. Exp Therm Fluid Sci. 2024;159(4):111272. doi:10.1016/j.expthermflusci.2024.111272.
12. Chau Pattnaik A, Samanta R, Chattopadhyay H. A brief on the application of multiphase lattice Boltzmann method for boiling and evaporation. J Therm Anal Calorim. 2022;148(7):2869–904. doi:10.1007/s10973-022-11820-8.
13. Luo KH, Fei L, Wang G. A unified lattice Boltzmann model and application to multiphase flows. Philosoph Transact Royal Soc A: Mathem Phys Eng Sci. 2021;379(2208):20200397. doi:10.1098/rsta.2020.0397.
14. Zhang C, Suekane T, Minokawa K, Hu Y, Patmonoaji A. Solute transport in porous media studied by lattice Boltzmann simulations at pore scale and X-ray tomography experiments. Phys Rev E. 2019;100(6):063110. doi:10.1103/physreve.100.063110.

15. Zarei A, Karimipour A, Meghdadi Isfahani AH, Tian Z. Improve the performance of lattice Boltzmann method for a porous nanoscale transient flow by provide a new modified relaxation time equation. Phys A: Stat Mech Applicat. 2019;535(2):122453. doi:10.1016/j.physa.2019.122453.
16. Kashani E, Mohebbi A, Feili Monfared AE, de Vries ET, Raoof A. Lattice Boltzmann simulation of dissolution patterns in porous media: single porosity versus dual porosity media. Adv Water Resour. 2024;188(1–3):104712. doi:10.1016/j.advwatres.2024.104712.
17. Sourya DP, Panda D, Kharaghani A, Tsotsas E, Gurugubelli PS, Surasani VK. Lattice Boltzmann simulations for the drying of porous media with gas-side convection-diffusion boundary. Phys Fluids. 2023 11;35(11):113324. doi:10.1063/5.0171573.
18. Inamuro T, Yoshino M, Suzuki K. An introduction to lattice boltzmann method: a numerical method for complex boundary and moving boundary flows. Singapore: World Scientific Publishing Co. Pte. Ltd.; 2022.
19. Strniša F, Urbic T. A lattice Boltzmann study of 2D steady and unsteady flows around a confined cylinder. J Braz Soc Mech Sci Eng. 2020;42(2):103. doi:10.1007/s40430-020-2176-y.
20. Marson F, Thorimbert Y, Chopard B, Ginzburg I, Latt J. Enhanced single-node lattice Boltzmann boundary condition for fluid flows. Phys Rev E. 2021;103(5):053308. doi:10.1103/physreve.103.053308.
21. Krüger T, Kusumaatmaja H, Kuzmin A, Shardt O, Silva G, Viggen E. The lattice boltzmann method: principles and practice. 1st ed. Cham, Switzerland: Springer International Publishing; 2017.
22. Yang JY, Dai XY, Xu QH, Liu ZY, Shi L, Long W. Lattice Boltzmann modeling of interfacial mass transfer in a multiphase system. Phys Rev E. 2021;104:015307. doi:10.1103/PhysRevE.104.015307.
23. Hu Y, Zhang S, He Q, Li D. Diffuse interface-lattice Boltzmann modeling for heat and mass transfer with Neumann boundary condition in complex and evolving geometries. Int J Heat Mass Transf. 2023;215(3):124480. doi:10.1016/j.ijheatmasstransfer.2023.124480.
24. Mapelli VP, Czelusniak LE, dos Santos Guzella M, Cabezas-Gómez L. Total energy thermal lattice boltzmann simulation of mixed convection in a square cavity. Int J Appl Comput Math. 2021;7(5):209. doi:10.1007/s40819-021-01147-7.
25. Shang B, Chen R, Yan W, Yu H. GPU accelerated volumetric lattice Boltzmann model for image-based hemodynamics in portal hypertension. Comput Fluids. 2023;266:106038. doi:10.1016/j.compfluid.2023.106038.
26. Meng W, Yang S, Lu X, Peng Y, Diao W, Zhang C. Lattice Boltzmann model and its GPU acceleration for transient flow in channel and pressurized pipe combined water delivery system. Appl Water Sci. 2025;15(3):60. doi:10.1007/s13201-025-02400-w.
27. Mei R, Yu D, Shyy W, Luo LS. Force evaluation in the lattice Boltzmann method involving curved geometry. Phys Rev E. 2002;65(4):041203. doi:10.1103/physreve.65.041203.
28. Lallemand P, Luo LS. Lattice Boltzmann method for moving boundaries. J Computat Phy. 2003;184(2):406–21. doi:10.1016/s0021-9991(02)00022-0.
29. Liu Y, Nie D. Lattice boltzmann simulation of flow past a finite cylinder. IOP Conf Ser: Mat Sci Eng. 2017;224(1):012021. doi:10.1088/1757-899X/224/1/012021.
30. Wang L, Liu Z, Rajamuni M. Recent progress of lattice Boltzmann method and its applications in fluid-structure interaction. Proc Institut Mech Eng Part C: J Mech Eng Sci. 2022;237(11):095440622210775. doi:10.1177/09544062221077583.
31. He X, Doolen G. Lattice boltzmann method on curvilinear coordinates system: flow around a circular cylinder. J Computat Phy. 1997;134(2):306–15. doi:10.1006/jcph.1997.5709.
32. Noble DR, Chen S, Georgiadis JG, Buckius RO. A consistent hydrodynamic boundary condition for the lattice Boltzmann method. Phys Fluids. 1995;7(1):203–9. doi:10.1063/1.868767.
33. Inamuro T, Yoshino M, Ogino F. A non-slip boundary condition for lattice Boltzmann simulations. Phys Fluids. 1995;7:2928–30. doi:10.1063/1.868766.

34. Behrend O. Solid-fluid boundaries in particle suspension simulations via the lattice Boltzmann method. Phys Rev E. 1995;52(1):1164–75. doi:10.1103/physreve.52.1164.
35. Filippova O, Hänel D. Grid refinement for lattice-BGK models. J Computat Physics. 1998;147(1):219–28. doi:10.1006/jcph.1998.6089.
36. Guo Z, Chu-Guang Z, Shi B. Non-equilibrium extrapolation method for velocity and boundary conditions in the lattice Boltzmann method. Chin Phys. 2002;11(6):366. doi:10.1063/1.1471914.
37. Tao S, He Q, Chen B, Yang X, Huang S. One-point second-order curved boundary condition for lattice Boltzmann simulation of suspended particles. Comput Mathem Applicat. 2018;76(7):1593–607. doi:10.1016/j.camwa.2018.07.013.
38. Izquierdo S, Martínez-Lera P, Fueyo N. Analysis of open boundary effects in unsteady lattice Boltzmann simulations. Comput Mathem Applicat. 2009;58(5):914–21. doi:10.1016/j.camwa.2009.02.014.
39. Mussa A, Asinari P, Luo LS. Lattice Boltzmann simulations of 2D laminar flows past two tandem cylinders. J Computati Phys. 2009;228(4):983–99. doi:10.1016/j.jcp.2008.10.010.
40. Lee C-H, Huang Z, Chiew Y-M. An extrapolation-based boundary treatment for using the lattice Boltzmann method to simulate fluid-particle interaction near a wall. Eng Applicat Computat Fluid Mech. 2015;9(1):370–81. doi:10.1080/19942060.2015.1061554.
41. Cheylan I, Favier J, Sagaut P. Immersed boundary conditions for moving objects in turbulent flows with the lattice-Boltzmann method. Phys Fluids. 2021;33(9):095101. doi:10.1063/5.0062575.
42. Romanus RS, Lugarini A, Franco AT. An immersed boundary-lattice Boltzmann framework for fully resolved simulations of non-spherical particle settling in unbounded domain. Comput Mathem Applicat. 2021;102(2):206–19. doi:10.1016/j.camwa.2021.10.018.
43. Nash RW, Carver HB, Bernabeu MO, Hetherington J, Groen D, Krüger T, et al. Choice of boundary condition for lattice-Boltzmann simulation of moderate-Reynolds-number flow in complex domains. Phys Rev E. 2014;89(2):023303. doi:10.1103/physreve.89.023303.
44. Hu K, Meng J, Zhang H, Gu XJ, Emerson DR, Zhang Y. A comparative study of boundary conditions for lattice Boltzmann simulations of high Reynolds number flows. Comput Fluids. 2017;156:1–8.
45. Martins IT, Alvarino PF, Cabezas-Gomez L. Lattice Boltzmann method for simulating transport phenomena avoiding the use of lattice units. J Braz Soc Mech Sci Eng. 2024;46(6):333. doi:10.1007/s40430-024-04905-y.
46. d'Humieres D. Generalized lattice-Boltzmann equations. In: Rarefied gas dynamics: theory and simulations; 1992. p. 450–8. doi:10.2514/5.9781600866319.0450.0458.
47. Lallemand P, Luo LS. Theory of the lattice Boltzmann method: dispersion, dissipation, isotropy, Galilean invariance, and stability. Phys Rev E. 2000;61(6):65463. doi:10.1103/physreve.61.6546.
48. Ladd AJC. Numerical simulations of particulate suspensions via a discretized Boltzmann equation. Part 2. Num Res J Fluid Mech. 1994;271:311–39. doi:10.1017/s0022112094001783.
49. Ladd AJC. Numerical simulations of particulate suspensions via a discretized Boltzmann equation. Part 1. Theor Found J Fluid Mech. 1994;271:285–309. doi:10.1017/s0022112094001771.
50. Ladd AJC, Verberg R. Lattice-Boltzmann simulations of particle-fluid suspensions. J Statist Physic. 2001;104(5–6):1191–251. doi:10.1023/A:1010414013942.
51. Chikatamarla SS, Ansumali S, Karlin IV. Grad's approximation for missing data in lattice Boltzmann simulations. Europhys Lett. 2006;74(2):215–21. doi:10.1209/epl/i2005-10535-x.
52. Yang Z. Lattice Boltzmann outflow treatments: convective conditions and others. Comput Mathem Applicat. 2013;65(2):160–71. doi:10.1016/j.camwa.2012.11.012.
53. Izquierdo S, Fueyo N. Characteristic nonreflecting boundary conditions for open boundaries in lattice Boltzmann methods. Phys Rev E. 2008;78(4):046707. doi:10.1103/physreve.78.046707.

54. Guo Z, Shu C. Lattice boltzmann method and its applications in engineering. Advances in computational fluid dynamics. World Scientific; 2013 [Internet]. [cited 2025 Jun 23]. Available from: https://books.google.com.br/books?id=I1llmwEACAAJ.
55. Tritton DJ. Experiments on the flow past a circular cylinder at low Reynolds numbers. J Fluid Mech. 1959;6(4):547–67. doi:10.1017/s0022112059000829.
56. Wieselsberger C. New data on the laws of fluid resistance; 1922 [Internet]. [cited 2025 Jun 23]. Available from: https://ntrs.nasa.gov/citations/19930080855.
57. Yuce MI, Kareem DA. A numerical analysis of fluid flow around circular and square cylinders. J AWWA. 2016;108(10):E546–54. doi:10.5942/jawwa.2016.108.0141.
58. Rajani BN, Kandasamy A, Majumdar S. Numerical simulation of laminar flow past a circular cylinder. Appl Mathem Modell. 2009;33(3):1228–47. doi:10.1016/j.apm.2008.01.017.
59. Ali A, Memon M, Bhatti K, Jacob K, Sitthiwirattham T, Promsakon C, et al. Modelling and simulation of fluid flow through a circular cylinder with high reynolds number: a COMSOL multiphysics study. J Math. 2022;2022(1):8. doi:10.1155/2022/5282980.
60. Perumal DA, Gundavarapu VS, Dass A. Lattice Boltzmann simulation of flow over a circular cylinder at moderate Reynolds numbers. Thermal Science. 2014;18(4):1235–46. doi:10.5402/2012/630801.
61. Tritton DJ. Physical fluid dynamics. Oxford, UK: Clarendon Press; 1977 [Internet]. [cited 2025 Jun 23]. Available from: https://books.google.com.br/books?id=reP_xhqZb2QC.

Appendix A Velocity Fields for $Re = 125$ and $t = 1500$ s

The velocity contours for each boundary scheme applied to the cylinder can be seen in Fig. A1, considering a Re of 125.

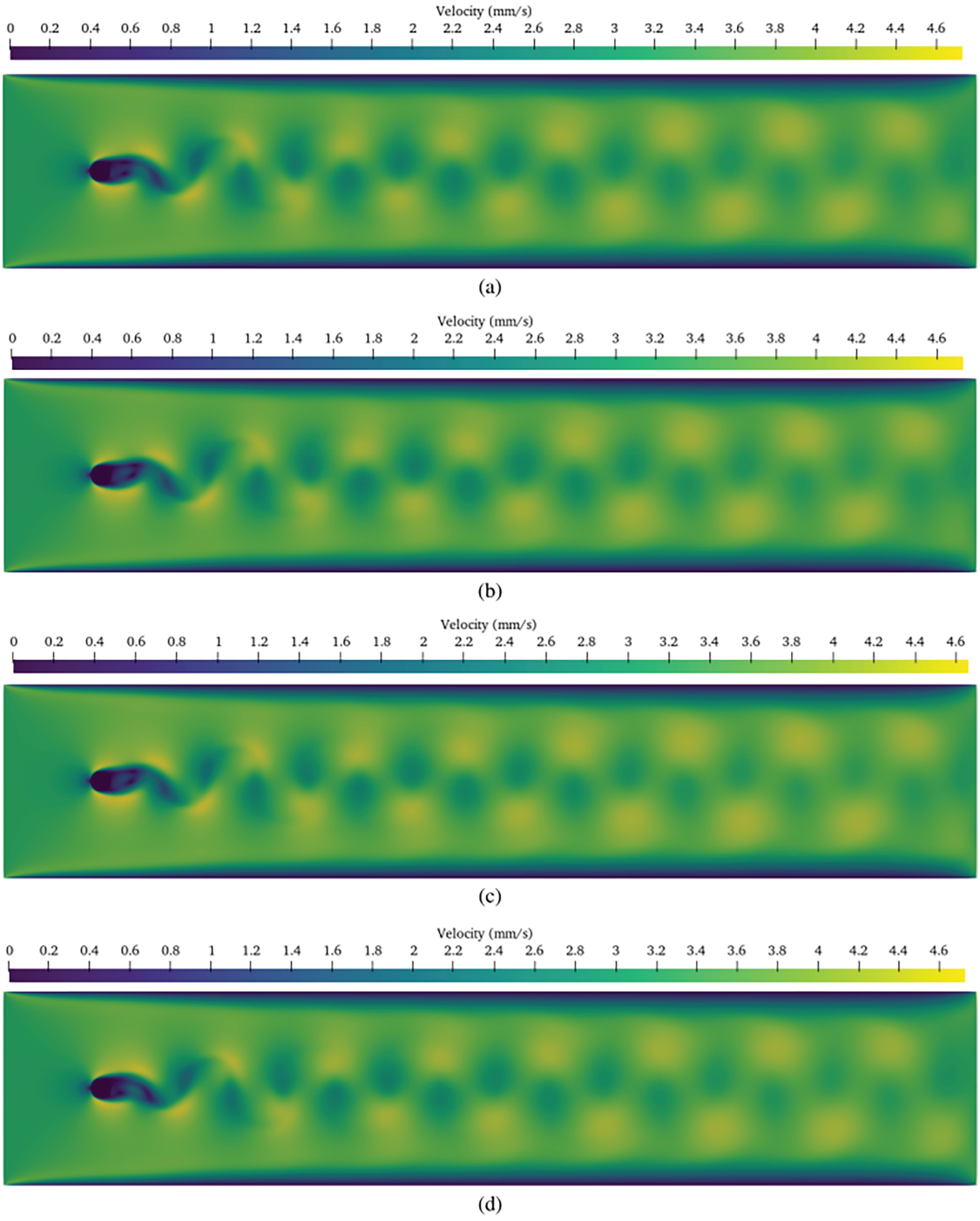

Figure A1: Velocity schemes for the (a) Standard bounce-back (b) Fictitious Equilibrium (c) Non-equilibrium extrapolation (d) One-point boundary condition schemes